Impact of textural patterns on rock weathering rates and size distribution of weathered grains

Yoni Israeli[1], Eyal Salhov[1], and Simon Emmanuel[1]

[1]The Institute of Earth Sciences, The Hebrew University of Jerusalem, Edmond J. Safra Campus, Givat Ram, Jerusalem 91904, Israel.

Corresponding author: Yoni Israeli (israeli.yoni@gmail.com)

Key Points:

- Numerical model simulating chemical weathering and grain detachment in rocks with different textural patterns.
- Weathering rate increases with increasing density of discontinuities.
- Mean size of detached fragments decreases with increasing tortuosity of the textural patterns.

Abstract

Rock texture has a critical influence over the way rocks weather. The most important textural factors affecting weathering are grain size and the presence of cracks and stylolites. These discontinuities operate as planes of mechanical weakness at which chemical weathering is enhanced. However, it is unclear how different rock textures impact weathering rates and the size of weathered grains. Here, we use a cellular automaton numerical model to simulate the weathering of rocks possessing grain boundaries, cracks, and stylolites. We ran simulations of both synthetic patterns as well as natural patterns of cracks, and stylolites. We found that for all patterns, weathering rates increase with the density of discontinuities. When the abundance of discontinuities was lower than ~25%, the synthetic patterns weathering rate followed the order: grid> honeycomb> Voronoi> brick-wall. However, for higher values of discontinuity density, all patterns exhibit similar weathering rates. We also tested the impact of the tortuosity of the pattern on weathering rates, and found rates to decrease with increasing tortuosity. In addition, we show that the rock textural pattern strongly impacts the detached grain size distributions. Rocks with an initial monomodal grain size distribution produce weathered fragments that are

normally distributed. In contrast, rocks with an initial log-normal size distribution produce weathered grains that are log-normally distributed. For the natural rock patterns we tested, weathering changed the initial multimodal grain size distributions to lower modality distributions.

Plain Language Summary

Rocks contain discontinuities such as voids and cracks. The number of these discontinuities and the patterns they form influence the resistance of rocks to chemical dissolution and mechanical decomposition. In this study, we built a computerized model that simulates how rocks with different patterns of discontinuities respond to contact with water. We found that rocks with a higher proportion of discontinuities eroded more rapidly than rocks with lower concentrations of discontinuities. In addition, we found that as the patterns became more interconnected, the weathering rate increased.

1 Introduction

Both natural and anthropogenic processes are affected by the rate at which rocks weather. Weathering rates impact the development of landscapes, the formation of soils, the fluid flow in aquifers and petroleum reservoirs, and the durability of buildings and monuments (Brantley, 2008; Dixon et al., 2012; Wilson, 2004). In addition, weathering rate plays a significant role in the global carbon cycle (Li & Elderfield, 2013; Torres et al., 2016), regulating atmospheric CO_2 on geological time scales (Them et al., 2017). Artificially accelerated weathering has even been suggested as a way of mitigating present-day anthropogenic carbon emissions (Beerling et al., 2020; Strefler et al., 2018; Torres et al., 2016; Xu & Liu, 2010).

Weathering rates are affected by both chemical and physical mechanisms. Rocks comprising minerals that are susceptible to chemical processes, such as dissolution, oxidation, and hydrolysis are expected to weather more rapidly than rocks comprising inert minerals (Buss et al., 2008; Critelli et al., 2014; Goldich, 1938; Maher et al., 2009; Nesbitt & Young, 1989; White & Buss, 2014). In addition, physical processes such as frost shattering, thermal expansion, and unloading (Eppes & Keanini, 2017; Hall, 1999; Matsuoka & Murton, 2008; Molnar, 2004; Park et al., 2015) can induce fracturing that causes mechanical weathering. Complicating matters

further, chemical and physical processes are often coupled (Anderson et al., 2004; Buss et al., 2008; Fletcher et al., 2006; Larsen et al., 2014; Røyne et al., 2008). As the density of cracks increases, more mineral surfaces are exposed to chemical reactions. At the same time, chemical dissolution along these cracks increases the overall porosity and weakens the rock mechanically (Brantley et al., 1990; Singhal & Gupta, 2010), accelerating physical weathering.

At the microscopic scale, weathering rates are affected by discontinuities that include crystalline defects, crystal edges and corners, and grain boundaries (Holdren & Speyer, 1987; Trindade Pedrosa et al., 2019). For example, the rate of dissolution along the edges and corners of a calcite spar was measured to be 1.7-3.6 faster than of the mineral face (Noiriel et al., 2019). In polycrystalline rocks, grain boundaries were found to be an order of magnitude more reactive than the bulk mineral (Bray et al., 2015; Emmanuel, 2014; Jonas et al., 2014). In studies focused on rock weathering at the submicron scale, enhanced dissolution at grain boundaries was shown to cause the mechanical detachment of particles into the fluid phase (Emmanuel & Levenson, 2014; Fischer & Luttge, 2017; Krklec et al., 2016; Silveira & Aarão Reis, 2013). Such chemo-mechanical rock weathering was observed in micritic limestone, (Levenson & Emmanuel, 2016), however, particle detachment can occur in various types of rocks with larger grain sizes and different mineral compositions (Israeli & Emmanuel, 2018; Krklec et al., 2013; Levenson & Emmanuel, 2016).

At macroscopic scales, rock weathering is accelerated by other types of discontinuities such as cracks, joints, fractures, and stylolites (Heap et al., 2018; Singhal & Gupta, 2010), which operate as planes of mechanical weakness and enhanced chemical weathering (Eppes & Keanini, 2017; Lei et al., 2017; Pacheco & Alencoão, 2006). For example, Røyne et al. (2008) showed that outcrop weathering is controlled by continual fracturing and production of surface area, which allows fluids to penetrate deeper into the rock and accelerate weathering rates.

While discontinuities are known to enhance weathering rates, the impact of different patterns and textures remains unclear. Discontinuities often show spatial ordering and fractal behavior (Babadagli, 2020; Ghosh & Daemen, 1993; Healy et al., 2017; Jafari & Babadagli, 2012; Liu et al., 2015), appearing in several superimposed networks reflecting the geological history of the rocks (Josnin et al., 2011; Singhal & Gupta, 2010). Typical patterns include conjugated sets of fractures, grid and ladder-like patterns, polygonal joints, and columnar joints

(Chan et al., 2008; Josnin et al., 2011; Singhal & Gupta, 2010). Furthermore, similar patterns can have different levels of connectivity depending on the spacing, orientation, length, and density of the discontinuities. The convolution of these factors can be represented by tortuosity, which is a measure of the geometric complexity of the pathways by which reactive fluids penetrate the rock. High tortuosity is expected to lead to reduced weathering rates, while low tortuosity could intensify weathering.

Here, we develop a cellular automaton model that simulates coupled chemo-mechanical weathering processes of rocks with different kinds of discontinuities and textural patterns. Specifically, we analyze the impact of the density and tortuosity of the discontinuities on the weathering rate. In addition, we examine how these parameters impact the size distribution of weathered rock fragments. We also discuss the implications for both surface and subsurface processes including soil and regolith production.

2 Methods and data

2.1 Model structure

To simulate the effects of chemo-mechanical weathering on rocks with different textures and grain size distributions, we used a model based on that described by Israeli and Emmanuel (2018). A 2-D cross-section of the rock was represented using a domain with 560*420 elements. Each element represented either a solid mineral, a discontinuity, or a fluid phase and is assigned a characteristic value.

In the simulations, chemical weathering only occurs in elements neighboring the fluid phase. In every time step, the probability that an element will dissolve depends both on the characteristic value of the element and the number of neighboring fluid elements. The dissolved elements are then reassigned as a fluid phase, and the domain is scanned for interconnected elements that are fully surrounded by fluid. These surrounded elements are considered to be detached physically and their elements are also reassigned to the fluid phase (Figure 1).

The discontinuities in the model are intended to represent grain boundaries, joints, cracks, or stylolites which are partially filled with cement. Thus, the discontinuities have an intrinsic strength that binds the rock together but they also dissolve more rapidly than the bulk rock, and this effect is included in the model.

The data from every simulation was saved as an object comprised of all the information from the simulation, including the rock's initial properties and the dynamic properties of the rock in every step. These properties include an image of the rock in every step, a list of pixels that were dissolved, location, and dimensions of detached fragments in every step. Using this object-oriented approach in Matlab™, each simulation takes several minutes on a standard PC and the data is uploaded into a MySQL database facilitating analysis of the datasets.

2.2 Patterns of discontinuities

In our model, we used two kinds of discontinuity patterns: synthetic and natural (Figure 2). Four different synthetic patterns were tested: (i) regular grid jointing; (ii) brick wall jointing; (iii) hexagonal jointing, simulating columnar patterns common in basalts; (iv) Voronoi tessellation, representing a coarse-grained crystalline rock. Weathering was also simulated for 4 natural rock patterns, obtained by binarization of outcrop images: (i) diagonal cracks; (ii) orthogonal cracks; (iii) stylolites oriented perpendicular to the weathering front; (iv) stylolites oriented sub-parallel to the weathering front. The crack patterns are taken from two locations: drone images from McDonald limestone in Scotland (Healy et al., 2017) and a limestone outcrop at the south margin of the Bristol Channel Basin, UK (Belayneh & Cosgrove, 2004). The stylolite patterns are derived from images of carbonate rocks from Israel, reported by Laronne Ben-Itzhak et al. (2014).

2.3 Model calculations

In the initial state of our simulations, we define a grain or block as a region bounded by discontinuities. We also define the discontinuity density as the proportion of discontinuity pixels in the domain. For natural rock patterns in our simulations, this varies in the range 2% to 30%, while for synthetic patterns this varies from 7% to 40%. For natural patterns, different values of discontinuity density were obtained by cropping the images. In simulations using synthetic patterns, discontinuity density is controlled by the number of grains in the domain: increasing the number of grains increases the discontinuity density.

Six different realizations were carried out for each pattern type, and a total of ~6000 simulations were completed. At each step, we calculated the number of elements removed by chemical weathering and by mechanical weathering. The dimensions and locations of each detached grain were recorded. The available reactive surface in every time step was also

147 calculated, based on the location of the pixels that neighbor the reactive fluid. The data were then
148 analyzed to assess the weathering rate and the grain size distribution of the detached fragments.
149 When calculating the grain size distributions, we only considered detached clusters larger than
150 10 pixels, and the amplitude of each size bin represents the cumulative number of pixels of the
151 individual grains within the bin. This approach is similar, but not identical, to grain size
152 distributions determined by mass in unconsolidated sediments and soils (Blott & Pye, 2001;
153 Konert & Vandenberghe, 1997).

154 For our model domains, we also calculated the tortuosity of the discontinuity patterns.
155 There are several different definitions of tortuosity (Hunt & Sahimi, 2017), and here, we adapted
156 the definition of Cooper et al. (2016) based on the convolution of diffusive transport flow paths:

157 $$(1)\ \tau = \epsilon \frac{D}{D^{\text{eff}}},$$

158 where ϵ is the discontinuity density, D is the intrinsic diffusivity of the discontinuity network,
159 while D^{eff} is the effective diffusivity through the bulk rock. We used the Tau Factor Matlab™
160 application (Cooper et al., 2016) to calculate the tortuosity based on our 2D images.

161

162 **3 Results and discussion**

163 3.1 Impact of discontinuity density on rock weathering rates

164 For all the rock patterns we tested, we found weathering rates to increase as the
165 discontinuity density increased (Figure 3). This result is not surprising since the dissolution rate
166 along the discontinuities is more rapid than the dissolution rate of the bulk rock. Moreover, this
167 is consistent with field and experimental observations of weathering rates in fractured rocks
168 (Eppes & Keanini, 2017; Røyne et al., 2008).

169 Our simulations also show that the type of discontinuity pattern has a significant impact
170 on weathering rates (Figure 3), particularly at discontinuity densities <25%. For the synthetic
171 patterns, at any given value of discontinuity density, the rates followed the order: grid>
172 honeycomb> Voronoi> brick wall. In natural rock patterns, the order was less clear, although
173 weathering in orthogonal cracks was faster than in diagonal cracks, and weathering in
174 perpendicular stylolites was faster than in parallel stylolites. In addition, synthetic patterns
175 generally weathered faster than natural rock patterns. This is probably due to the irregular nature
176 of natural patterns and their inherently lower connectivity.

177 At discontinuity densities >25%, the weathering rates of all the patterns begin to
178 converge. This may be because at low discontinuity densities, the tortuosity of the pathways and
179 their low connectivity acts as a limiting factor. As the discontinuity density increases,
180 connectivity is expected to increase, facilitating the advance of the weathering front. Although
181 the discontinuity density is a critical parameter in determining weathering rates, our results
182 suggest that additional parameters related to the geometry of the patterns are also likely to impact
183 the way rocks weather. Specifically, for patterns in which the pathways are highly tortuous and
184 poorly connected, rates are expected to be slower.

185 3.2 Impact of tortuosity on weathering rates

186 In the simulations of synthetic rocks, each pattern type showed a decrease in weathering
187 rate with increasing tortuosity (Figure 4a). Moreover, the rates grouped into two distinct trends:
188 (i) grid and brick wall, and (ii) honeycomb and Voronoi. This is probably due to the similarity in
189 the geometry of the patterns within each trend. By contrast, for natural rock patterns, there is no
190 clear dependence of weathering rate on tortuosity for individual pattern types (Figure 4b). This
191 could be related to the irregularity and anisotropy of discontinuities in natural patterns, which
192 can cause patterns with identical tortuosities to behave differently. In addition, the widely
193 varying discontinuity densities in the natural patterns could also mask the apparent impact of
194 tortuosity.

195 To isolate the impact of tortuosity, we conducted a numerical experiment with
196 simulations of synthetic patterns in which tortuosity changed systematically while maintaining
197 the same level of discontinuity density (Figure 5). Starting with a regular grid, we introduced an
198 offset in alternating layers to create brick wall patterns, which increased the tortuosity. In this
199 method, the tortuosity varied from 1.95-2.75. In each offset, we ran six simulations with 3
200 different initial grain sizes: 2160, 234, and 108 pixels.

201 Our results show a near-linear decrease in the weathering rate as the tortuosity increases
202 from 1.95 to 2.75 (Figure 6) for all the three grain sizes tested. Overall, the reduction in rate was
203 33%, 21%, and 27% for the 2160, 234, and 108 grain size simulations, respectively. This
204 significant effect means that in addition to mineralogy and grain size, the tortuosity of the
205 discontinuity pattern is likely to be a critical factor in determining the weathering rate in real
206 rocks.

3.3 Impact of discontinuity density and tortuosity on size of detached grains:

We found the mean detached grain size decreases non-linearly with increasing discontinuity density for both synthetic and natural patterns (Figure 7). For the synthetic patterns, the detachment grain size drops by approximately 90% as the discontinuity density increases from 8% to 25% (Figure 7a). For natural patterns, there is a significant level of variability and the trend is far less clear (Figure 7b). This is most likely a result of the differences between the initial conditions in the synthetic patterns and those in the natural patterns: in the synthetic patterns, the initial grain sizes are similar for any given discontinuity density, while in natural patterns, the initial grain size varies significantly.

The overall reduction of the mean detached fragment size with increasing discontinuity density is caused by two factors. The first is that increasing discontinuity density leads to a reduction in the initial grain size, which results in smaller detached grains. The second is that as the discontinuity density increases, the chemical weathering rate also increases, causing the grains to undergo more dissolution prior to detachment.

To test if tortuosity plays a role in the size of detached grains, we analyzed the results of the offset experiment described in Section 3.2 and found that the mean detachment size decreases with increasing tortuosity (Figure 8). This is because in patterns with higher tortuosity, chemical dissolution has longer time to act and reduce the size of the grains prior to detachment. This effect can be seen in the simulation snapshots in Figure 5: detaching grains in the grid simulation are larger than the detaching grains in the offset simulations.

3.4 Impact of textural patterns on the size distribution of weathered grains

In all the rock patterns we tested, the grain size distribution of detached blocks was influenced by the rock textural patterns. For the synthetic patterns possessing an *initial* uniform grain size (grid, honeycomb, brick-wall), the *detached* grains showed a normal size distribution (Figure 9 a-c). By contrast, for Voronoi patterns, the detached grain size distribution was log-normal, similar to the initial grain size distribution (Figure 9d). For the natural rock patterns we tested (stylolites and cracks), the initial block size distributions were multimodal. However, the size distribution of the detached fragments showed reduced modality (Figure 10). Our results are consistent with the findings of Palomares et al. (1993) who showed that rocks with similar initial grain sizes fragment mainly along their uniformly distributed discontinuities, thus providing

grains of uniform size, in contrast to rocks with anisotropic fabrics that do not disintegrate uniformly.

Grain size distributions of weathered grains strongly influence soil permeability and soil erosion (Cohen et al., 2015). Soils with a wide range of grain sizes are less permeable and erode less readily than soils with uniform grain size distributions (Cohen et al., 2015). Thus, we expect rocks with initial grid-like, or honeycomb discontinuity patterns to produce relatively uniform grain size distributions that form soils with higher permeabilities. By contrast, rocks with stylolites and cracks might be expected to produce soils that form impermeable layers.

Although there is significant variability, the grain size distribution of many soils and sediments often has a log-normal distribution (Gardner, 1956; Wagner & Ding, 1994). In our simulations, the only pattern that weathered into fragments with log-normal distributions is the Voronoi pattern. These patterns are common in the polycrystalline rocks that provide much of the weathered material to sediments, and it is likely that the log-normal distribution in sediments is influenced by the initial grain size distribution of the weathered rock. However, transport processes also strongly affect the size distributions of sediments, (Hunt & Sahimi, 2017), and we therefore expect the discontinuity patterns to have the strongest impact on the distribution of sediments that are relatively close to the source rock, such as in fluvial fans.

4 Conclusions

In this study, we used a numerical model that incorporates both chemical and mechanical weathering to investigate the impact of rock texture on weathering rate and the size of detached grains. Our results indicate that the weathering rate increases with increasing densities of discontinuities in the rock. We also found that increasing the tortuosity of the patterns lead to decreasing weathering rates. Moreover, we found a strong impact of texture on the detached grain size distribution, and that higher discontinuity densities leads to smaller detached blocks. This has practical implications for risk assessment near cliffs or stone edifices: rocks containing stylolites with spacings of several centimeters could present less of a risk than rocks containing fractures with spacings of tens of centimeters.

The model we present here is a preliminary attempt to simulate the combined effects of chemical and mechanical weathering, and we can identify some limitations to our approach. Our

simulations compare textures of different scales: the individual grains comprising a rock are often micrometer or millimeter in scale, while joints and stylolites are often present at the centimeter and meter-scale. Moreover, the time and spatial scales in the model are at present arbitrary, which severely limits its predictive power. Calibrating the model, however, requires reliable field data, which are difficult to obtain because of the long time scales associated with weathering. Future work that focuses on improving the model by comparison with field-based measurements could provide solutions to some of these challenges.

Acknowledgments and Data

This research was supported by student scholarships from the Israeli Water Authority, the Rieger Foundation, and the Hebrew University Advanced School of Environmental Studies. The Israel Science Foundation is thanked for their generous support. The dataset for this research is publicly available in the Mendeley Data repository at DOI: http://dx.doi.org/10.17632/v4jw2d9rbm.1 (Israeli, 2020).

References

Anderson, S. P., Blum, J., Brantley, S. L., Chadwick, O., Chorover, J., Derry, L. A., Drever, J. I., Hering, J. G., Kirchner, J. W., Kump, L. R., Richter, D., & White, A. E. (2004). Proposed initiative would study Earth's weathering engine. *Eos, Transactions American Geophysical Union*, *85*(28), 265-269. https://doi.org/10.1029/2004eo280001

Babadagli, T. (2020). Unravelling transport in complex natural fractures with fractal geometry: A comprehensive review and new insights. *Journal of Hydrology*, *587*, 124937. https://doi.org/https://doi.org/10.1016/j.jhydrol.2020.124937

Beerling, D. J., Kantzas, E. P., Lomas, M. R., Wade, P., Eufrasio, R. M., Renforth, P., Sarkar, B., Andrews, M. G., James, R. H., Pearce, C. R., Mercure, J.-F., Pollitt, H., Holden, P. B., Edwards, N. R., Khanna, M., Koh, L., Quegan, S., Pidgeon, N. F., Janssens, I. A., Hansen, J., & Banwart, S. A. (2020). Potential for large-scale CO2 removal via enhanced rock weathering with croplands. *Nature*, *583*(7815), 242-248. https://doi.org/10.1038/s41586-020-2448-9

Belayneh, M., & Cosgrove, J. W. (2004). Fracture-pattern variations around a major fold and their implications regarding fracture prediction using limited data: an example from the Bristol Channel Basin. *Geological Society, London, Special Publications*, *231*(1), 89-102. https://doi.org/10.1144/gsl.sp.2004.231.01.06

Blott, S. J., & Pye, K. (2001). GRADISTAT: a grain size distribution and statistics package for the analysis of unconsolidated sediments. *Earth surface processes and Landforms*, *26*(11), 1237-1248.

Brantley, S. L. (2008). Kinetics of Mineral Dissolution. In S. L. Brantley, J. D. Kubicki, & A. F. White (Eds.), *Kinetics of Water-Rock Interaction* (pp. 151-210). Springer New York. https://doi.org/10.1007/978-0-387-73563-4_5

Brantley, S. L., Evans, B., Hickman, S. H., & Crerar, D. A. (1990). Healing of microcracks in quartz: Implications for fluid flow. *Geology*, *18*(2), 136-139. https://doi.org/10.1130/0091-7613(1990)018<0136:homiqi>2.3.co;2

Bray, A. W., Oelkers, E. H., Bonneville, S., Wolff-Boenisch, D., Potts, N. J., Fones, G., & Benning, L. G. (2015). The effect of pH, grain size, and organic ligands on biotite weathering rates. *Geochimica et Cosmochimica Acta*, *164*, 127-145. https://doi.org/10.1016/j.gca.2015.04.048

Buss, H. L., Sak, P. B., Webb, S. M., & Brantley, S. L. (2008). Weathering of the Rio Blanco quartz diorite, Luquillo Mountains, Puerto Rico: Coupling oxidation, dissolution, and fracturing. *Geochimica et Cosmochimica Acta*, *72*(18), 4488-4507. https://doi.org/http://dx.doi.org/10.1016/j.gca.2008.06.020

Chan, M. A., Yonkee, W. A., Netoff, D. I., Seiler, W. M., & Ford, R. L. (2008). Polygonal cracks in bedrock on Earth and Mars: Implications for weathering. *Icarus*, *194*(1), 65-71. https://doi.org/https://doi.org/10.1016/j.icarus.2007.09.026

Cohen, S., Willgoose, G., Svoray, T., Hancock, G., & Sela, S. (2015). The effects of sediment transport, weathering, and aeolian mechanisms on soil evolution. *Journal of Geophysical Research: Earth Surface*, *120*(2), 260-274. https://doi.org/10.1002/2014jf003186

Cooper, S. J., Bertei, A., Shearing, P. R., Kilner, J. A., & Brandon, N. P. (2016). TauFactor: An open-source application for calculating tortuosity factors from tomographic data. *SoftwareX*, *5*, 203-210. https://doi.org/https://doi.org/10.1016/j.softx.2016.09.002

Critelli, T., Marini, L., Schott, J., Mavromatis, V., Apollaro, C., Rinder, T., De Rosa, R., & Oelkers, E. H. (2014). Can the dissolution rates of individual minerals be used to describe whole rock dissolution? EGU General Assembly Conference Abstracts,

Dixon, J. L., Hartshorn, A. S., Heimsath, A. M., DiBiase, R. A., & Whipple, K. X. (2012). Chemical weathering response to tectonic forcing: A soils perspective from the San Gabriel Mountains, California. *Earth and Planetary Science Letters*, *323-324*, 40-49. https://doi.org/https://doi.org/10.1016/j.epsl.2012.01.010

Emmanuel, S. (2014). Mechanisms influencing micron and nanometer-scale reaction rate patterns during dolostone dissolution. *Chemical Geology*, *363*, 262-269. https://doi.org/http://dx.doi.org/10.1016/j.chemgeo.2013.11.002

Emmanuel, S., & Levenson, Y. (2014). Limestone weathering rates accelerated by micron-scale grain detachment. *Geology*, *42*(9), 751-754.

Eppes, M.-C., & Keanini, R. (2017). Mechanical weathering and rock erosion by climate-dependent subcritical cracking. *Reviews of Geophysics*, *55*(2), 470-508. https://doi.org/10.1002/2017rg000557

Fischer, C., & Luttge, A. (2017). Beyond the conventional understanding of water–rock reactivity. *Earth and Planetary Science Letters*, *457*, 100-105. https://doi.org/https://doi.org/10.1016/j.epsl.2016.10.019

Fletcher, R., Buss, H., & Brantley, S. (2006). A spheroidal weathering model coupling porewater chemistry to soil thicknesses during steady-state denudation. *Earth and Planetary Science Letters*, *244*(1-2), 444-457. https://doi.org/10.1016/j.epsl.2006.01.055

Gardner, W. (1956). Representation of soil aggregate-size distribution by a logarithmic-normal distribution1, 2. *Soil Science Society of America Journal*, *20*(2), 151-153.

Ghosh, A., & Daemen, J. J. K. (1993). Fractal characteristics of rock discontinuities. *Engineering Geology*, *34*(1), 1-9. https://doi.org/https://doi.org/10.1016/0013-7952(93)90039-F

Goldich, S. S. (1938). A Study in Rock-Weathering. *The Journal of Geology*, *46*(1), 17-58. https://doi.org/10.1086/624619

Hall, K. (1999). The role of thermal stress fatigue in the breakdown of rock in cold regions. *Geomorphology*, *31*(1), 47-63. https://doi.org/https://doi.org/10.1016/S0169-555X(99)00072-0

Healy, D., Rizzo, R. E., Cornwell, D. G., Farrell, N. J., Watkins, H., Timms, N. E., Gomez-Rivas, E., & Smith, M. (2017). FracPaQ: A MATLAB™ toolbox for the quantification of fracture patterns. *Journal of Structural Geology*, *95*, 1-16.

Heap, M., Reuschlé, T., Baud, P., Renard, F., & Iezzi, G. (2018). The permeability of stylolite-bearing limestone. *Journal of Structural Geology*, *116*, 81-93. https://doi.org/https://doi.org/10.1016/j.jsg.2018.08.007

Holdren, G. R., & Speyer, P. M. (1987). Reaction rate-surface area relationships during the early stages of weathering. II. Data on eight additional feldspars. *Geochimica et Cosmochimica Acta*, *51*(9), 2311-2318. https://doi.org/https://doi.org/10.1016/0016-7037(87)90284-5

Hunt, A. G., & Sahimi, M. (2017). Flow, Transport, and Reaction in Porous Media: Percolation Scaling, Critical-Path Analysis, and Effective Medium Approximation. *Reviews of Geophysics*, *55*(4), 993-1078. https://doi.org/10.1002/2017rg000558

Israeli, Y. (2020). *Dataset of Israeli et al 2020-Impact of textural patterns on rock weathering rates and size distribution of weathered grains* Version V1). https://doi.org/10.17632/v4jw2d9rbm.1

Israeli, Y., & Emmanuel, S. (2018). Impact of grain size and rock composition on simulated rock weathering. *Earth Surf. Dynam.*, *6*(2), 319-327. https://doi.org/10.5194/esurf-6-319-2018

Jafari, A., & Babadagli, T. (2012). Estimation of equivalent fracture network permeability using fractal and statistical network properties. *Journal of Petroleum Science and Engineering*, *92-93*, 110-123. https://doi.org/https://doi.org/10.1016/j.petrol.2012.06.007

Jonas, L., John, T., King, H. E., Geisler, T., & Putnis, A. (2014). The role of grain boundaries and transient porosity in rocks as fluid pathways for reaction front propagation. *Earth and Planetary Science Letters*, *386*, 64-74. https://doi.org/https://doi.org/10.1016/j.epsl.2013.10.050

Josnin, J.-Y., Jourde, H., Pascal, F., & Bidaux, P. (2011). A three-dimensional model to simulate joint networks in layered rocks. *Canadian Journal of Earth Sciences*, *39*, 1443-1455. https://doi.org/10.1139/e02-043

Konert, M., & Vandenberghe, J. (1997). Comparison of laser grain size analysis with pipette and sieve analysis: a solution for the underestimation of the clay fraction. *Sedimentology*, *44*(3), 523-535.

Krklec, K., Domínguez-Villar, D., Carrasco, R. M., & Pedraza, J. (2016). Current denudation rates in dolostone karst from central Spain: Implications for the formation of unroofed caves. *Geomorphology*, *264*, 1-11. https://doi.org/http://dx.doi.org/10.1016/j.geomorph.2016.04.007

Krklec, K., Marjanac, T., & Perica, D. (2013). Analysis of "standard" (Lipica) limestone tablets and their weathering by carbonate staining and SEM imaging, a case study on the Vis Island, Croatia. *Acta Carsologica*, *42*(1), 135-142.

Laronne Ben-Itzhak, L., Aharonov, E., Karcz, Z., Kaduri, M., & Toussaint, R. (2014). Sedimentary stylolite networks and connectivity in limestone: Large-scale field observations and implications for structure evolution. *Journal of Structural Geology*, *63*, 106-123. https://doi.org/https://doi.org/10.1016/j.jsg.2014.02.010

Larsen, I. J., Almond, P. C., Eger, A., Stone, J. O., Montgomery, D. R., & Malcolm, B. (2014). Rapid Soil Production and Weathering in the Southern Alps, New Zealand. *Science*, *343*(6171), 637-640. https://doi.org/10.1126/science.1244908

Lei, Q., Latham, J.-P., & Tsang, C.-F. (2017). The use of discrete fracture networks for modelling coupled geomechanical and hydrological behaviour of fractured rocks. *Computers and Geotechnics*, *85*, 151-176.

Levenson, Y., & Emmanuel, S. (2016). Quantifying micron-scale grain detachment during weathering experiments on limestone. *Geochimica et Cosmochimica Acta*, *173*, 86-96.

Li, G., & Elderfield, H. (2013). Evolution of carbon cycle over the past 100 million years. *Geochimica et Cosmochimica Acta*, *103*, 11-25. https://doi.org/https://doi.org/10.1016/j.gca.2012.10.014

Liu, R., Jiang, Y., Li, B., & Wang, X. (2015). A fractal model for characterizing fluid flow in fractured rock masses based on randomly distributed rock fracture networks. *Computers and Geotechnics*, *65*, 45-55. https://doi.org/https://doi.org/10.1016/j.compgeo.2014.11.004

Maher, K., Steefel, C. I., White, A. F., & Stonestrom, D. A. (2009). The role of reaction affinity and secondary minerals in regulating chemical weathering rates at the Santa Cruz Soil Chronosequence, California. *Geochimica et Cosmochimica Acta*, *73*(10), 2804-2831. https://doi.org/https://doi.org/10.1016/j.gca.2009.01.030

Matsuoka, N., & Murton, J. (2008). Frost weathering: recent advances and future directions. *Permafrost and Periglacial Processes*, *19*(2), 195-210. https://doi.org/10.1002/ppp.620

Molnar, P. (2004). Interactions among topographically induced elastic stress, static fatigue, and valley incision. *Journal of Geophysical Research: Earth Surface*, *109*(F2). https://doi.org/10.1029/2003jf000097

Nesbitt, H. W., & Young, G. M. (1989). Formation and Diagenesis of Weathering Profiles. *The Journal of Geology*, *97*(2), 129-147. https://doi.org/10.1086/629290

Noiriel, C., Oursin, M., Saldi, G., & Haberthür, D. (2019). Direct Determination of Dissolution Rates at Crystal Surfaces Using 3D X-ray Microtomography. *ACS Earth and Space Chemistry*, *3*(1), 100-108. https://doi.org/10.1021/acsearthspacechem.8b00143

Pacheco, F. A. L., & Alencoão, A. M. P. (2006). Role of fractures in weathering of solid rocks: narrowing the gap between laboratory and field weathering rates. *Journal of Hydrology*, *316*(1), 248-265. https://doi.org/https://doi.org/10.1016/j.jhydrol.2005.05.003

Palomares, M., Arribas, J., Johnsson, M. J., & Basu, A. (1993). Modern stream sands from compound crystalline sources: Composition and sand generation index. In *Processes Controlling the Composition of Clastic Sediments* (Vol. 284, pp. 0). Geological Society of America. https://doi.org/10.1130/SPE284-p313

Park, J., Hyun, C. U., & Park, H. D. (2015). Changes in microstructure and physical properties of rocks caused by artificial freeze–thaw action [Article]. *Bulletin of Engineering Geology and the Environment*, *74*(2), 555-565. https://doi.org/10.1007/s10064-014-0630-8

Røyne, A., Jamtveit, B., Mathiesen, J., & Malthe-Sørenssen, A. (2008). Controls on rock weathering rates by reaction-induced hierarchical fracturing. *Earth and Planetary Science Letters*, *275*(3), 364-369. https://doi.org/https://doi.org/10.1016/j.epsl.2008.08.035

Silveira, F. A., & Aarão Reis, F. D. A. (2013). Detachment of non-dissolved clusters and surface roughening in solid dissolution. *Electrochimica Acta*, *111*, 1-8. https://doi.org/http://dx.doi.org/10.1016/j.electacta.2013.08.007

Singhal, B. B. S., & Gupta, R. P. (2010). Fractures and Discontinuities. In B. B. S. Singhal & R. P. Gupta (Eds.), *Applied Hydrogeology of Fractured Rocks: Second Edition* (pp. 13-33). Springer Netherlands. https://doi.org/10.1007/978-90-481-8799-7_2

Strefler, J., Amann, T., Bauer, N., Kriegler, E., & Hartmann, J. (2018). Potential and costs of carbon dioxide removal by enhanced weathering of rocks. *Environmental Research Letters*, *13*(3), 034010.

Them, T. R., Gill, B. C., Selby, D., Gröcke, D. R., Friedman, R. M., & Owens, J. D. (2017). Evidence for rapid weathering response to climatic warming during the Toarcian Oceanic Anoxic Event. *Scientific Reports*, *7*(1), 5003. https://doi.org/10.1038/s41598-017-05307-y

Torres, M. A., West, A. J., Clark, K. E., Paris, G., Bouchez, J., Ponton, C., Feakins, S. J., Galy, V., & Adkins, J. F. (2016). The acid and alkalinity budgets of weathering in the Andes–Amazon system: Insights into the erosional control of global biogeochemical cycles. *Earth and Planetary Science Letters*, *450*, 381-391. https://doi.org/https://doi.org/10.1016/j.epsl.2016.06.012

Trindade Pedrosa, E., Kurganskaya, I., Fischer, C., & Luttge, A. (2019). A Statistical Approach for Analysis of Dissolution Rates Including Surface Morphology. *Minerals*, *9*(8), 458.

Wagner, L. E., & Ding, D. (1994). Representing aggregate size distributions as modified lognormal distributions. *Transactions of the ASAE*, *37*(3), 815-821.

White, A. F., & Buss, H. L. (2014). Natural Weathering Rates of Silicate Minerals. *Treatise on Geochemistry (Second Edition), Elsevier, Oxford*, 115-155. https://doi.org/10.1016/b978-0-08-095975-7.00504-0

Wilson, M. J. (2004). Weathering of the primary rock-forming minerals: processes, products and rates. *Clay Minerals*, *39*(3), 233. https://doi.org/10.1180/0009855043930133

Xu, Z., & Liu, C.-Q. (2010). Water geochemistry of the Xijiang basin rivers, South China: Chemical weathering and CO2 consumption. *Applied Geochemistry*, *25*(10), 1603-1614. https://doi.org/https://doi.org/10.1016/j.apgeochem.2010.08.012

Figure 1:

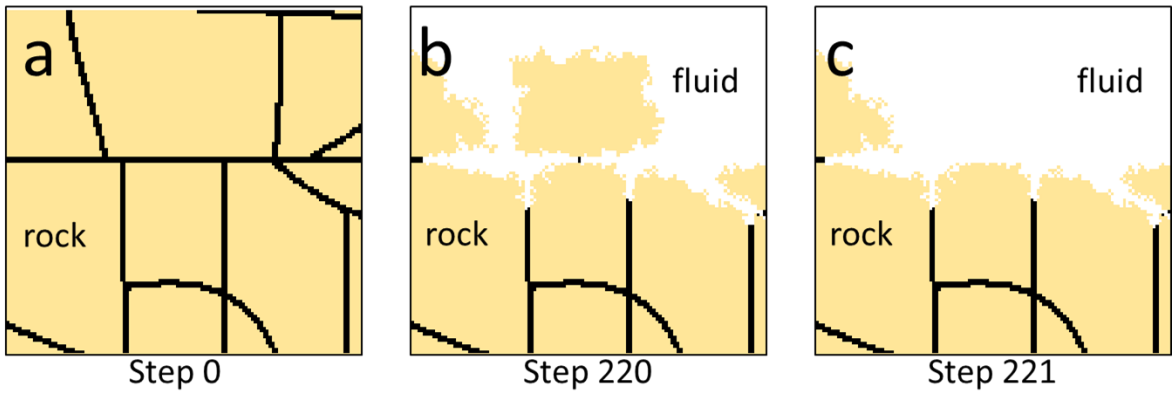

Figure 1. Simulation of fluid-rock interaction. The bulk rock components are marked in yellow, rock discontinuities in black, and fluid in white. Cross sections of the rock are shown at 3 stages of the simulation: (a) initial state; (b) Step 220 and (c) Step 221. Chemical weathering dissolves the rock minerals slower than the discontinuities between rock clusters. When a cluster is surrounded by fluid it detaches from the surface and is removed from the simulation. Note that the black discontinuities dissolve more rapidly than the bulk rock.

Figure 2.

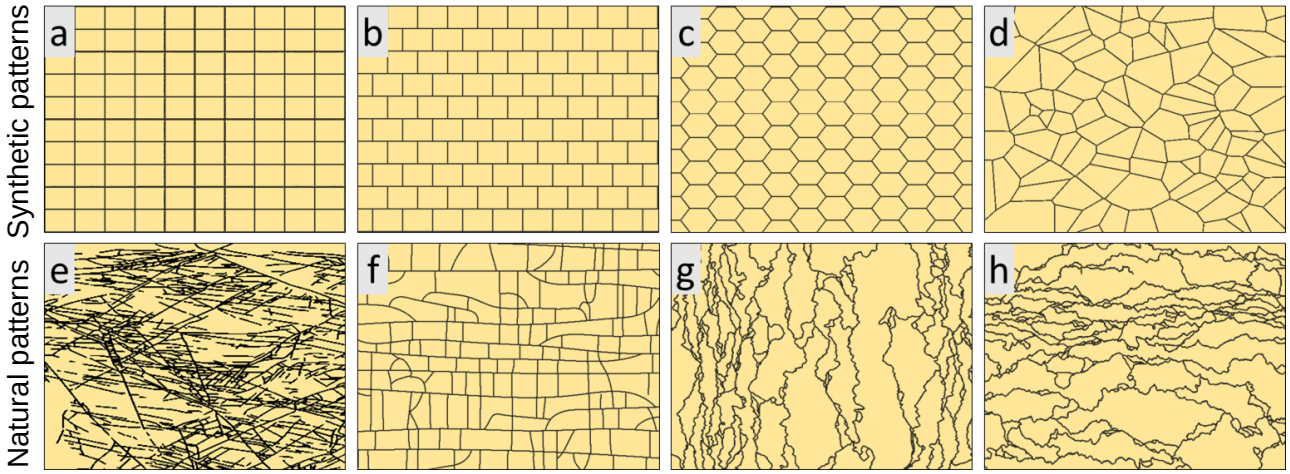

Figure 2. Examples of synthetic and natural rock patterns used in the simulations. The upper row represents synthetic rock textures of a grid (a), brick-wall (b), honeycomb (c) and realistic polycrystalline rock (Voronoi, d). The lower row is our model representation for natural rock images of diagonal cracks (e), orthogonal cracks (f), perpendicular stylolites (g), and parallel stylolites (h).

Figure 3.

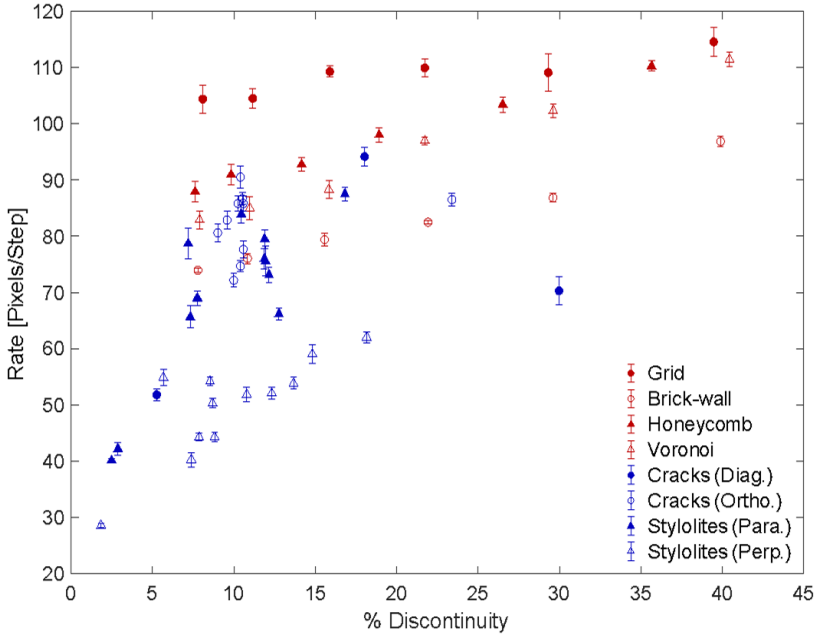

Figure 3. Weathering rate as a function of discontinuity density in synthetic (red) and natural (blue) patterns. Each of the synthetic patterns shows a linear increase in weathering rate with the density of discontinuities. In the natural rock patterns, the trend is less clear. At lower discontinuity density, the weathering rate exhibits a strong dependence on the pattern.

Figure 4.

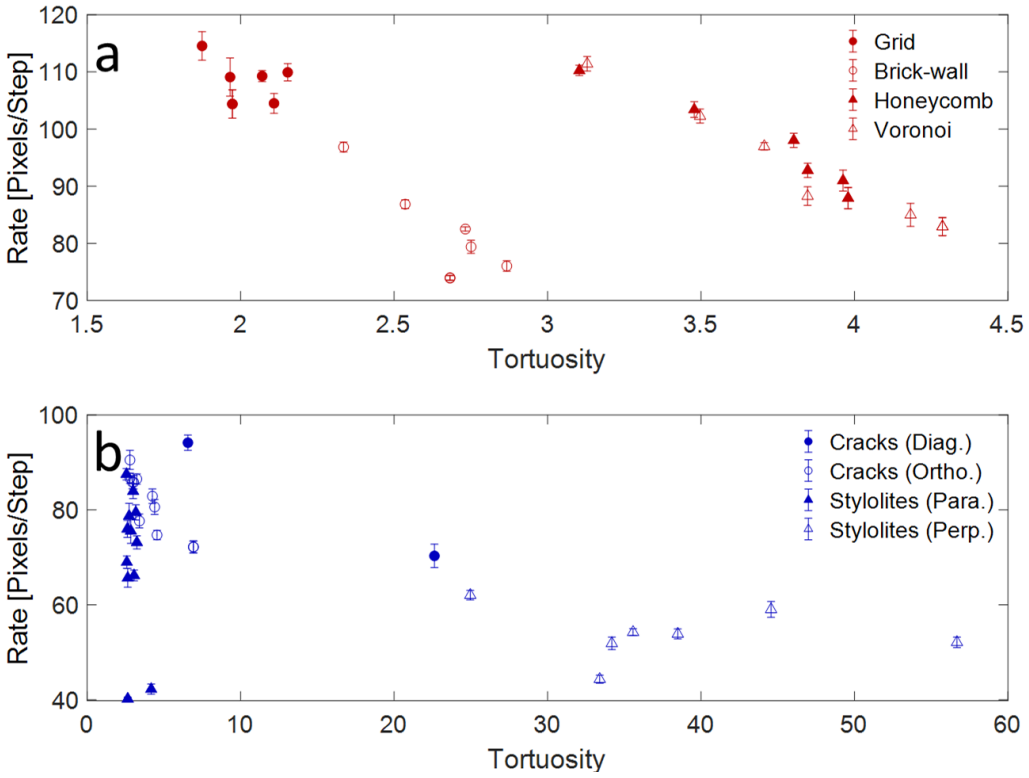

Figure 4. Weathering rate as a function of tortuosity in (a) synthetic patterns and (b) and natural patterns. In the synthetic patterns there are two distinct groups. In the synthetic patterns, there are two distinct trends, in contrast to the natural patterns, which show no clear relationship.

Figure 5.

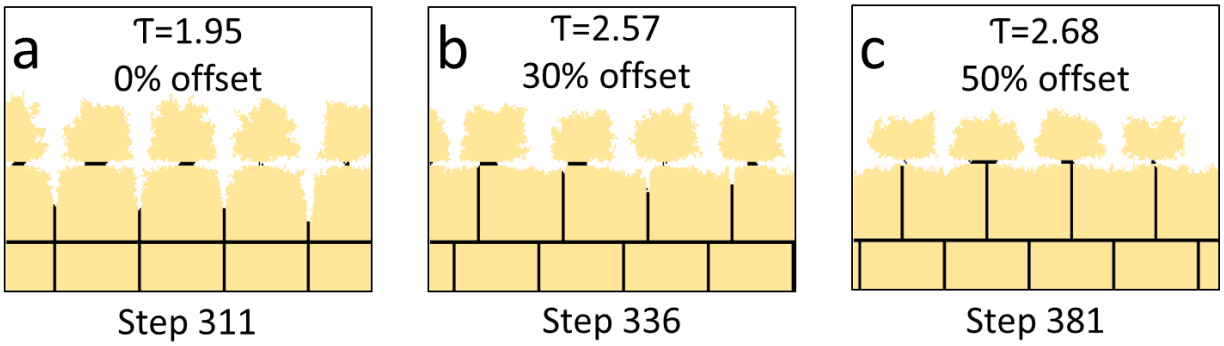

Figure 5. Snapshots of 3 simulations with different offsets and tortuosities. Each image shows the times step directly preceding a grain detachment event. The initial grain size is μ_0=2160 pixels. Note the decrease in size of detached grains and in the difference in patterns of penetration of the reactive fluid into the rock. In addition, for the lowest level tortuosity the reaction front advances much more rapidly than at higher levels of tortuosity.

Figure 6.

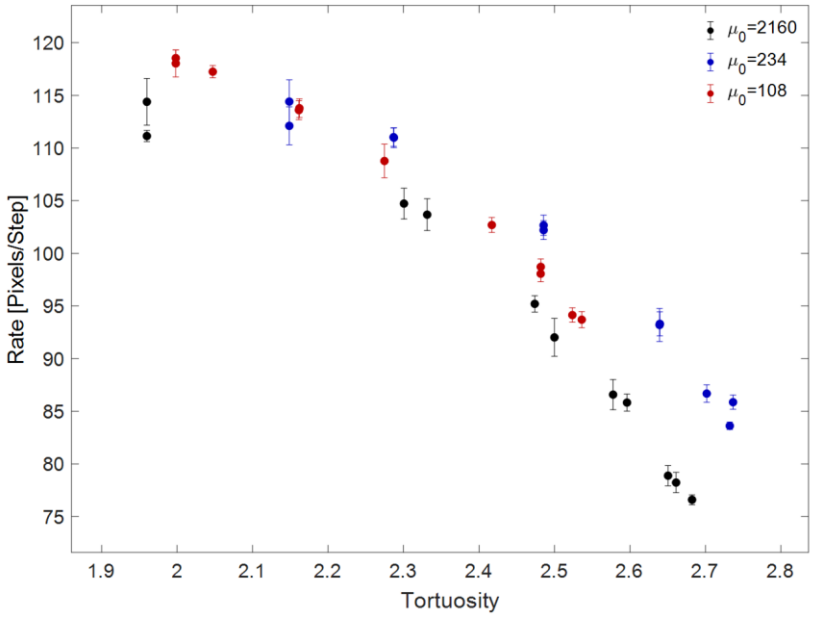

Figure 6. Weathering rate versus tortuosity in simulations with offset from grid (0% offset) to brick-wall (50% offset) and back to grid (100% offset), in three decreasing initial grain sizes μ_0=2160 pixels (black), μ_0=234 pixels (blue) and μ_0=108 pixels (red).

Figure 7.

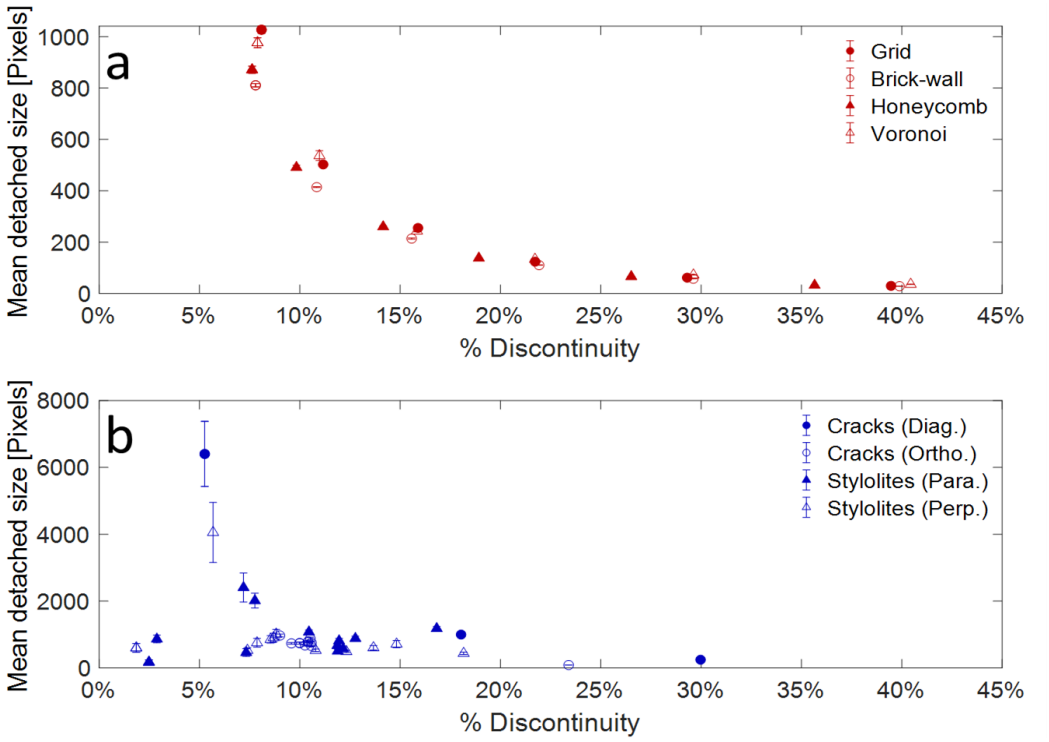

Figure 7. Impact of discontinuity density on mean detachment size in (a) synthetic and (b) natural patterns. The synthetic patterns show a non-linear reduction in detachment grain size with increasing discontinuity density. In the natural patterns, the discontinuity abundance is less systematic, but the trend is similar.

Figure 8.

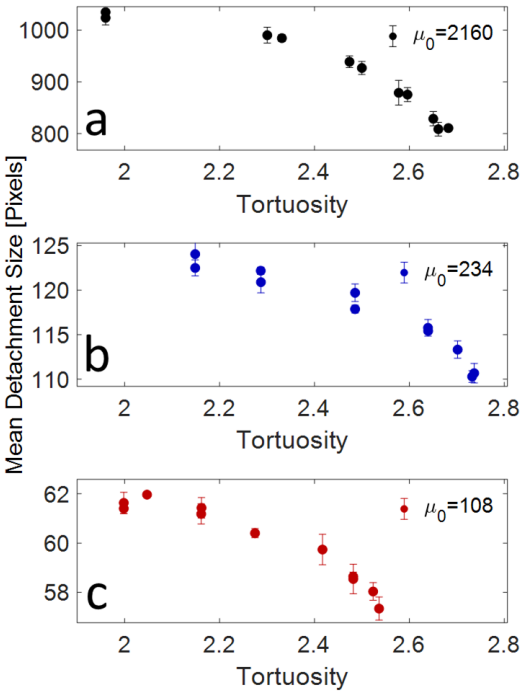

Figure 8. Mean detachment size as a function tortuosity in offset simulations for 3 initial grain sizes pixels (a) 2160 pixels; (b) 234 pixels; and (c) 108 pixels.

Figure 9.

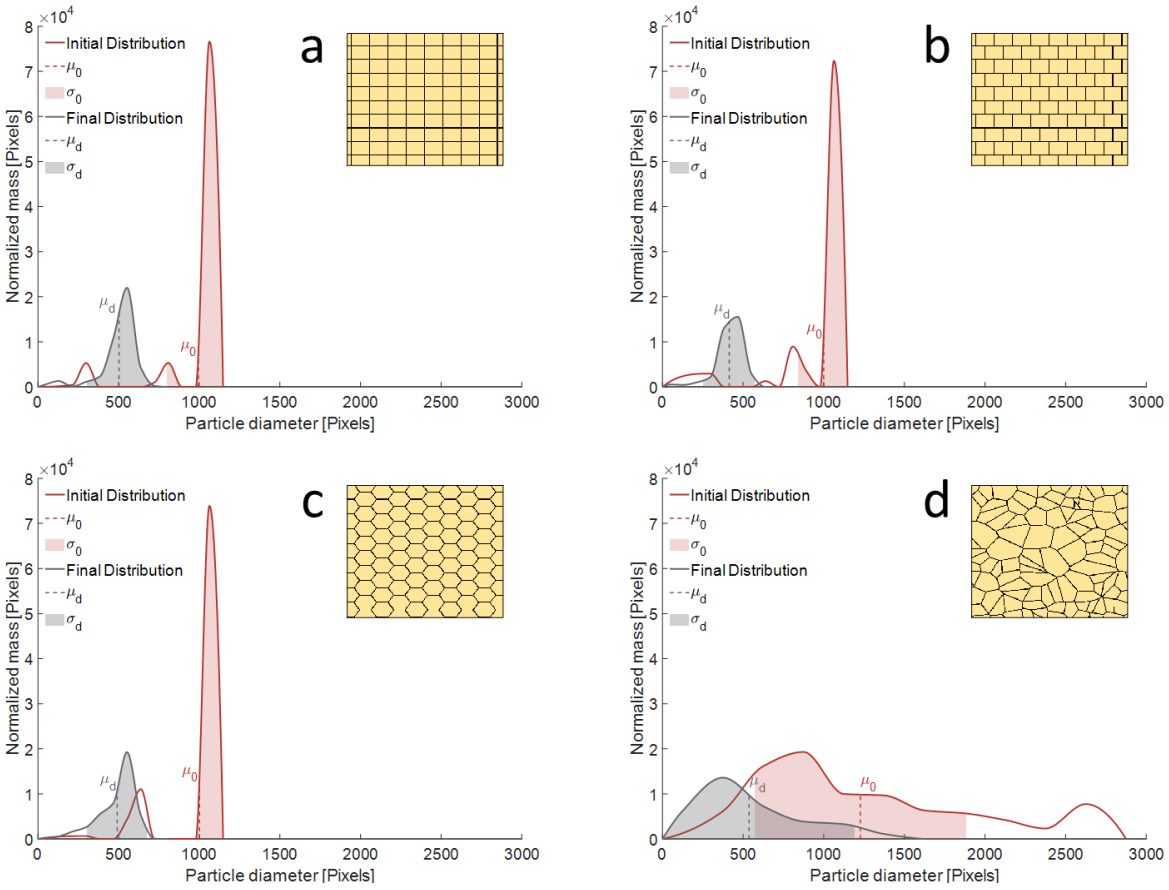

Figure 9. Initial grain size distribution and size distribution of detached grains for synthetic rock patterns: (a) grid; (b) brick-wall; (c) honeycomb; and (d) Voronoi patterns. The initial distribution is shown by the solid red line, with the mean initial grain size indicated by the dashed red line. The standard deviation from the mean is shown by the shaded region. The size distribution of the detached grains is indicted by the solid gray line. The mean detached grain size is shown by the dashed gray line, and the standard deviation from the mean is indicated by the area shaded in gray.

Figure 10.

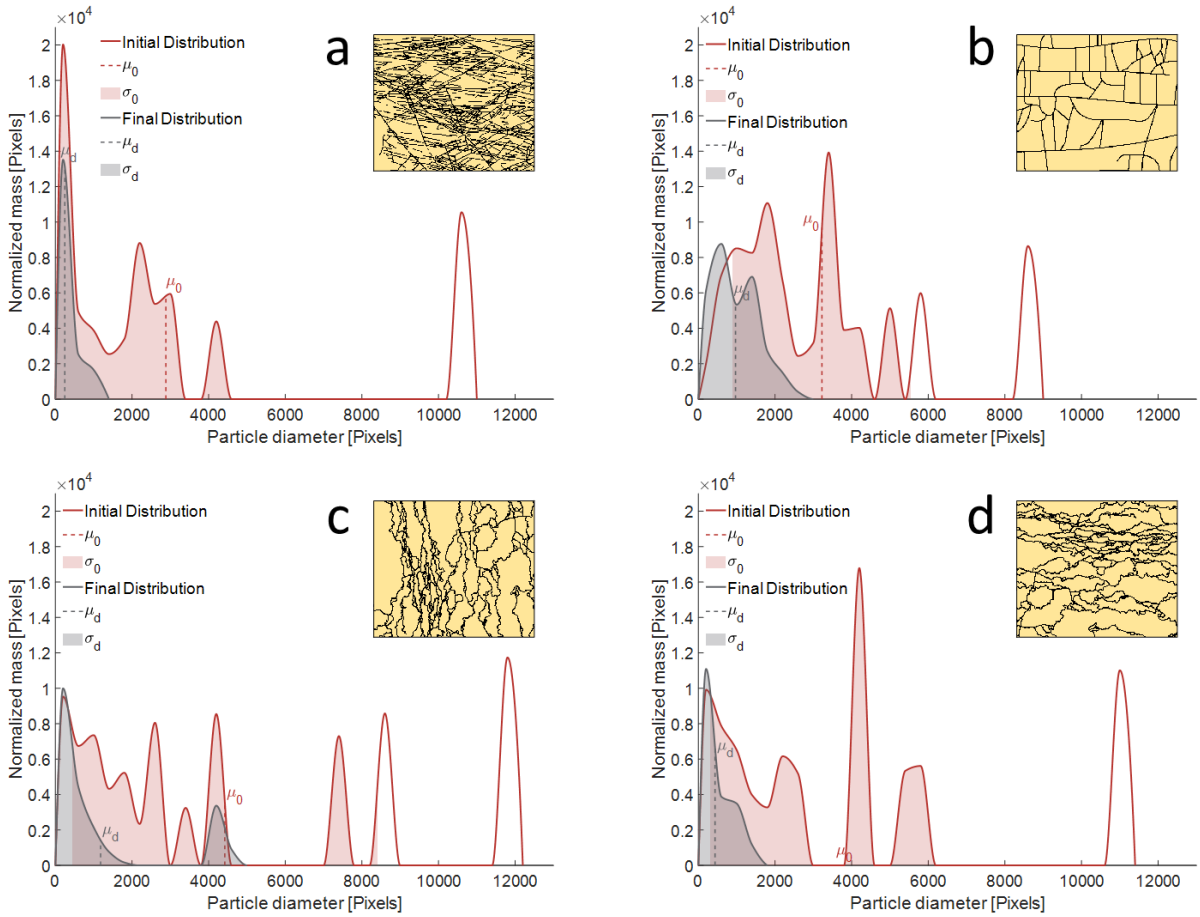

Figure 10. Initial grain size distribution and size distribution of detached grains for natural rock patterns: (a) diagonal cracks; (b) orthogonal cracks; (c) perpendicular stylolites; and (d) and parallel stylolites. The initial distribution is shown by the solid red line, with the mean initial grain size indicated by the dashed red line. The standard deviation from the mean is shown by the pink shaded region. The size distribution of the detached grains is indicted by the solid gray line. The mean detached grain size is shown by the dashed gray line, and the standard deviation from the mean is indicated by the area shaded in gray. The weathering process decreases the modality of the distribution in all tested natural patterns.